A CROSS-SENSOR-BASED APPROACH TO ESTIMATE DEPTH VALUES IN NEARSHORE COASTAL WATERS, CASE STUDY: NAYBAND BAY, PERSIAN GULF

K. Kabiri [1] * , M. Moradi[1]

[1] Dept. of Marine Remote Sensing, Iranian National Institute for Oceanography and Atmospheric Science, Tehran, Iran - *kabiri@inio.ac.ir

Commission IV, WG IV/3

KEY WORDS: Remote Sensing, Bathymetry, Landsat-8 OLI, Sentinel-2 MSI, Multispectral Satellite Images

ABSTRACT:

A cross-sensor-based approach using Landsat-8 OLI (L8/OLI) and Sentinel-2A MSI (S2A/MSI) imagers was examined to estimate bathymetric data in nearshore coastal waters. An L8/OLI image and an S2A/MSI image (Acquisition date: November 16, 2017) were selected from Nayband Bay, the southern region of Iran. In addition, precise bathymetric data for the studied area were used to calibrate the models and validate the results. Ratio together with traditional linear transform methods and a novel cross-sensor-based method were conducted to determine the depth values from both satellite images. Four bands of L8/OLI imager (Band No.1: Coastal/Aerosol [0.435-0.451 µm], Band No. 2: blue [0.452-0.512 µm], Band No. 3: green [0.533-0.590 µm], and Band No. 4: red [0.636-0.673 µm], spatial resolution: 30 m) were considered to create the aforementioned models while the three bands of S2A/ MSI imager were used (Band No. 2: blue [0.458-0.523 µm], Band No. 3: green [0.543-0.578 µm], and Band No. 4: red [0.650-0.680 µm], spatial resolution: 10 m). All models' accuracy was evaluated using comparing the calculated bathymetric information with field observed values. The statistical indicators including correlation coefficients (R^2), root mean square errors (*RMSE*), and standard errors (*SE*) for validation points were computed for all models of two imagers. The final results demonstrated that although the spatial resolution of L8/OLI imagery is less than S2A/MSI, the precision of estimated depth is higher due to having more bands in the visible wavelength range. However, the integrated cross-sensor-based method including the bands of both sensors yielded the most accurate results (R^2 = 0.90, *RMSE*= 1.66 m, and *SE* =1.29 m).

1. INTRODUCTION

The accessibility of up-to-date and consistent depth data in near-shore coastal waters is crucial for monitoring and supervision of coastal areas and for recording the benthic habitats (Chust et al., 2010; Kabiri et al., 2013; Kabiri et al., 2014; Kabiri et al., 2018) Several methods so far have been settled to compute the depth values and subsequently to produce the bathymetric maps. Although, the most precise and reliable methods are conducting the single or multi-beam echo sounders (Maleika et al., 2012; Horta et al., 2014) and airborne LIght Detection And Ranging (LIDAR) (Chust et al. 2010; Sayla et al., 2017), they are yet most costly methods as well. The other main usage of the depth data, is for mapping the coral reefs in the shallow coastal areas with high spatial resolution satellite images (Samimi Namin et al., 2009). This means that in absence of high resolution and precise bathymetric data, the other low-cost and more available methods should be examined to estimate depth values in nearshore coastal areas for mapping the benthic habitats and for management of coastal areas.

On the other hand, the remotely sensed satellite images have shown their capabilities for mapping and monitoring the marine and nearshore coastal areas (Kabiri et al., 2016; Kabiri et al., 2017; Kabiri, 2020; Kabiri et al., 2020; Kabiri 2022a & b). Lyzenga (1978) initialized a methodology to extract the depth values from multispectral satellite images. Thereafter, Stumpf et al. (2003) developed a ratio transform method with higher abilities for calculation of depth values in deeper areas. Although after 2000, the new generation of high spatial resolution imagery (Pixel size < 4m) such as Ikonos, QuickBird, and WorldView enabled us to produce high accuracy and more detailed bathymetric maps (Collin and Planes, 2011; Euegenio et al., 2015; Halls and Costin, 2016; Manessa et al., 2016), these images are costly and cover a small area in a unique scene. On the other hand, the lower spatial resolution satellite images such as Landsat (SGD= 30 m) are in access since 1985 and can be applied to yield medium resolution depth data (Clark et al., 1987; Baban, 1993; Liceaga-Correa and Euan-Avila, 2002). This ability has been further improved after the launch of Landsat-8 on February 2013 (Pahlevan et al., 2014; Pacheco et al., 2015). Recently, Sentinel-2A & -2B satellites have launched with 10 m spatial resolution in visible bands and show their ability to produce more detailed and precise bathymetric map (Kabiri, 2017; Evagorou et al., 2019; Yunus et al., 2019).

This study is an attempt to evaluate the capability of a novel cross-sensor-based methodology, including Sentinel-2A MSI (S2A/MSI) and landsat-8 OLI (L8/OLI) imagers to determine depth values in near-shore coastal waters. To do so, Nayband Bay (located in the south of Iran, northern Persian Gulf) was nominated as the study area, due to accessibility to a reliable and precise bathymetric information. This data allowed us to calibrate the methods for calculation of depth values and then to assess their accuracies as well. Firstly, the ratio and linear transformations developed by Stumpf et al. (2003) were used to determine depth values from two images separately, to calculate the depth values in each point. Afterward, a novel cross-sensor-based method was initialized, so that combined the bands of both sensors. This innovative method was then compared with

* Corresponding author

traditional methods to understand whether it can enhance the calculated depth data or not. The optimal technique was then nominated by comparison of the statistical indices, including *RMSE* (Root mean square error), R^2 (correlation coefficient), and also *SE* (Standard error) for the determined depth values for all aforesaid methods.

2. MATERIALS AND METHODS

2.1 Study Site

Nayband Bay is located in the north of the Persian Gulf between latitudes 27° 23′ N–27° 30′ N and longitudes 52° 35′ E–52° 41′ E (Figure 1). The area and perimeter of this bay are ~70 km^2 and ~40 km respectively. The deeper parts (~20 m) occurred in the western areas, where the depth of mid parts is ~10 m. The type of water of Nayband Bay classifies as Case II coastal waters, i.e., the water clarity is lower than the Case I waters (Open-ocean). However, in comparison with summertime, the turbidity of water in the studied area usually is less than in wintertime, hence it is decided to utilize satellite images acquired on wintertime (Ghobadi et al., 2015a). The study area is affected by sand storms (Ghafarian et al., 2022) and its climate is changing rapidly (Ghobadi et al., 2015b; Beni et al., 2021). The weather system of Nayband Bay is sub-tropical which means high temperature and humidity in summertime.

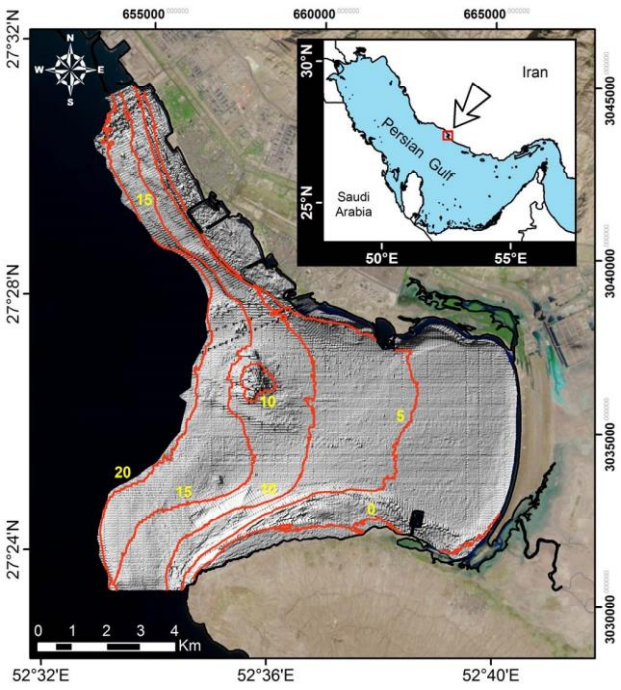

Figure 1. Bathymetric information of the Nayband Bay in the southern Iran. Projection system is UTM-Zone 39 (WGS-84)

2.2 Remote Sensing Satellite Data

In this study, it was decided to employ medium spatial resolution (10 to 30 m) satellite images, where they are available to download with no cost. To do so, two clouds free S2A/MSI and L8/OLI satellite images (acquired on November 16, 2017) were selected and then downloaded from the USGS (United States Geological Survey) EarthExplorer website (https://earthexplorer.usgs.gov/). It should be mentioned that, since the revisit cycle of Landsat-8 And Sentinel-2 satellites are 16 and 5 days respectively, we will have a harmonised overpass of them in each 80 days. However, the changes in topography of benthic area is not much rapid and it will be enough to have bathymetric data with a 80-day time interval to assess the benthic habitats and features. Moreover, the Landsat-9 satellite is recently launched with the images similar to the Landsat-8, which means the method developed in this study, may be used on them as well.

At the first step, the raw satellite images should be corrected in the primary step, before satellite data may be utilized for next procedures. These pre-processing are including atmospheric, radiometric, and geometric rectifications. In this study, the essential image analyses were conducted using ENVI® 5.6 image processing software. Firstly, radiance values were computed from the raw digital numbers (DN). Afterward, the FLAASH® (fast line-of-sight atmospheric analysis of hypercubes) module was applied to implement required atmospheric correction. It should be noted that the output of this phase will be the reflectance values in absence of atmospheric interference for each pixel of the images. Although, there are some other modules to perform atmospheric correction for L8/OLI and S2A/MSI imagers such as ACOLITE and Sen2Cor, our investigations revealed that the quality of FLAASH module is enough for our purpose in this research, where the remain errors after atmospheric corrections will be minimised after applying parametric transformations to estimate depth values. Thereafter, a geometric correction was implemented for both satellite images and they were resampled based on coordinates of some ground control points to improve geometric properties and for consistency between them and bathymetric data as well.

2.3 Field Observed Depth Data

An in-situ measurement was practiced by the [Iranian] National Cartographic Center (NCC) in 2013 to generate a hydrographic map for Nayband Bay. The depth values were measured with a single beam echo-sounder powered by DGPS (differential global positioning system), which means the precision and accuracy of observed data are adequate to produce bathymetric maps at the scale of 1:1000 (Figure 2). For this research, the source of surveyed sounding points was employed for further analysis. Thereafter, the depth values edited based on the tidal regime of the Nayband Bay (extracted from NCC, Department of Hydrography) exactly in the same time of the satellite's overpasses. Thereafter, to conduct comparison analyses, the vector-based point-wise depth data were transformed to a raster-based ArcGIS raster data, for being consistent with geometric specifications (pixel size and also coordinate system) of the aforementioned S2A/MSI and L8/OLI imagers. As seen in Figure 2, to produce a high precision map, the distance of sounding points is lesser in the regions with coarse topography and more in the areas with smoother topography. It should be mentioned that, since the field data are observed in 2013 and the satellite data obtained in 2017, there should be some inconsistency between them, however our analyses show that these differences are rare and negligible in most areas. The hydrographic data also were used to perform geometric corrections on both imagers, where many ground control points were selected to conduct resampling procedure.

This contribution has been peer-reviewed. The double-blind peer-review was conducted on the basis of the full paper.
https://doi.org/10.5194/isprs-annals-X-4-W1-2022-343-2023 | © Author(s) 2023. CC BY 4.0 License.

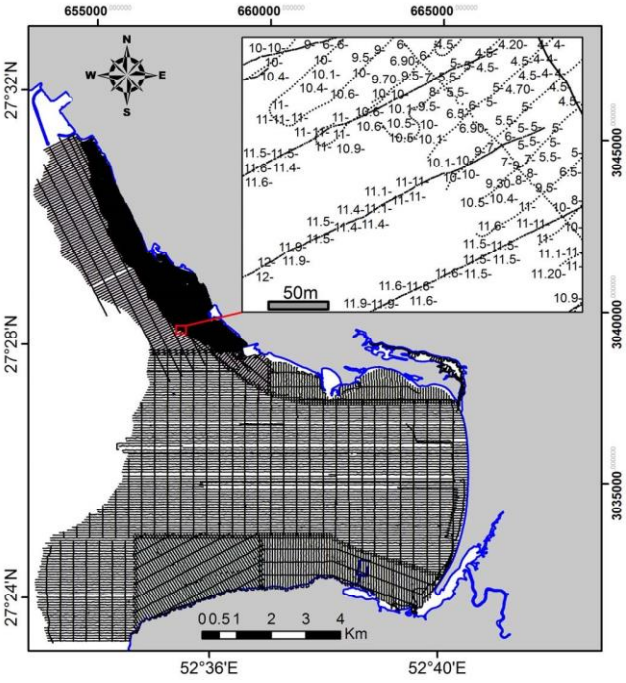

Figure 2. The hydrographic sounding points measured by single beam echo-sounder. The distance of sounding points is less in the regions with coarse topography and more in areas with smoother topography

2.4 Extraction of Depth Data from the Multispectral Bands of Both Satellites

Both the linear transform method for calculation of depth data from satellite imagery introduced by Lyzenga (1978, 1981) and then the ratio transform method was improved by Stumpf et al. (2003). In this study, the capabilities of both methods were evaluated by integration of three visible bands of S2A/MSI imager (Band 2: blue (0.4580.523 µm), Band 3: green (0.543-0.578 µm), and Band 4: red (0.65-68 µm)) and four bands of L8/OLI imager (Band 1: Coastal/Aerosol (0.435-0.451 µm), Band 2: blue (0.4520.512 µm), Band 3: green (0.533-0.59 µm), and Band 4: red (0.636-0.673 µm). It should be noted that the spatial resolution of S2A/MSI and L8/OLI are 10 m and 30 m respectively (in visible bands). Based on the linear transformation, the depth data (Z) can be determined by (1)

$$Z = a_0 + a_1 X_R + a_2 X_G + a_3 X_B + a_4 X_{CB} \quad (1)$$

where:

$$X_i = \ln[R_w(\lambda_i) - R_\infty(\lambda_i)] \quad (2)$$

The X_j, and X_k values may be computed by equations same as (2). In these equations, R_w is the reflectance of water including the bottom reflectance in shallow areas, R_∞ is the reflectance of deep areas (reflectance of water column), and λ_i is the i^{th} spectral band. It means to calculate depth values, the unknown a values (a_0 to a_n, n = number of spectral bands) must be computed in advance. The R_∞ values for all chosen bands of both sensors were calculated by considering the mean reflectance values of pixels within a deep area (Depth > 20 m). Consequently, determined reflectance values are 0.19, 1.57, and 2.12 for R, G, and B bands of S2A/MSI, and are considered as R_∞^R, R_∞^G, and R_∞^B, respectively. These values are 1.82, 2.89, 3.59, and 4.92 for L8/ OLI for R, G, B, and CB bands. Since there is not an ability for penetration of light for any of the abovementioned bands at depths of more than 15 m; hence, the regions deeper than 15 m were masked from analyses. Furthermore, any pixels including of undesirable features such as clouds and boats were filtered (Figure 3). Consequently, the number of pixels were ~65000 for L8/OLI and ~585000 for S2A/MSI. Half of these points was used to conduct calculation of unknown parameters and the others was remained for evaluation of the models. As instance, Figure 3 shows these points for selected L8/OLI image.

The ratio transform method is formed based on the ratio values of visible bands. In this study, the traditional formulation was extended to include all visible bands of S2A/MSI and L8/OLI images. Consequently, the depth data may be determined by utilizing (3).

$$Z = -m_0 + m_1 \frac{\ln(\mathrm{nR_w}(\lambda_{CB}))}{\ln(\mathrm{nR_w}(\lambda_B))} + m_2 \frac{\ln(\mathrm{nR_w}(\lambda_{CB}))}{\ln(\mathrm{nR_w}(\lambda_G))} + m_3 \frac{\ln(\mathrm{nR_w}(\lambda_{CB}))}{\ln(\mathrm{nR_w}(\lambda_R))} + m_4 \frac{\ln(\mathrm{nR_w}(\lambda_B))}{\ln(\mathrm{nR_w}(\lambda_G))} + m_5 \frac{\ln(\mathrm{nR_w}(\lambda_B))}{\ln(\mathrm{nR_w}(\lambda_R))} + m_6 \frac{\ln(\mathrm{nR_w}(\lambda_G))}{\ln(\mathrm{nR_w}(\lambda_R))} \quad (3)$$

Where parameters m_1–m_6 are adjustable parameters to scale the ratio to depth, n is a fixed value for all extents (here n=100), and m_0 is the offset for a depth= 0 m. The unknown values of m_i parameters were calculated using linear regression method. Finally, the depth of all points that selected to validate the results (same as previous method) were determined using (3) for both S2A/MSI and L8/OLI images.

In the next step, the possible development in accuracy and precision of the estimated depth values was inspected by examining a cross-sensor-based model based on combination of the two aforesaid satellite images (4). Same as the aforementioned transformations, the unknown parameters (m_i) were estimated with linear regression to four particular cross-sensor-based models (including two linear and two ratio transforms). The results found from these models were then related to the ratio and linear transformation, and the statistical indices such as correlation coefficient (R^2), *RMSE*, and standard errors (*SE*) were determined for all of 8 models. Since the number of bands (and consequently the band ratios) for both imagers are not too many, all of them are considered to be involved in the integrated cross-sensor-based algorithm.

$$Z = -m_0 + m_1 \frac{ln(nR_w(\lambda_{CB}))}{ln(nR_w(\lambda_B))} + m_2 \frac{ln(nR_w(\lambda_{CB}))}{ln(nR_w(\lambda_G))} + m_3 \frac{ln(nR_w(\lambda_{CB}))}{ln(nR_w(\lambda_R))} + m_{4S2A} \frac{ln(nR_w(\lambda_B))}{ln(nR_w(\lambda_G))} + m_{5S2A} \frac{ln(nR_w(\lambda_B))}{ln(nR_w(\lambda_R))} + m_{6S2A} \frac{ln(nR_w(\lambda_G))}{ln(nR_w(\lambda_R))} + m_{4L8} \frac{ln(nR_w(\lambda_B))}{ln(nR_w(\lambda_G))} + m_{5L8} \frac{ln(nR_w(\lambda_B))}{ln(nR_w(\lambda_R))} + m_{6L8} \frac{ln(nR_w(\lambda_G))}{ln(nR_w(\lambda_R))} \quad (4)$$

Model No.	Bands	Linear transform									
		a_0	a_1	a_2	a_3	a_4	*SE*	R^2	*RMSE*		
S2A/MSI											
1	R- G- B	12.29	3.97	-6.89	0.31		1.71	0.82	2.908		
L8/OLI											
2	R- G- B	13.08	3.71	-8.19	1.37		1.73	0.82	2.980		
3	R- G- B- CB	12.39	2.27	-6.17	-3.58	4.37	1.68	0.83	2.809		
S2A/MSI & L8/OLI											
4	R- G- B (S2A)	12.79	3.32	-4.08	0.39	4.04	1.59	0.85	2.528		
	R- G- B- CB (L8)		1.36	-2.69	-3.41						
	Band Ratios	Ratio transform							*SE*	R^2	*RMSE*
		m_0	m_1	m_2	m_3	m_4	m_5	m_6			
S2A/MSI											
5	B/G- B/R- G/R	815.10				850.76	-613.71	588.21	2.51	0.62	6.28
L8/OLI											
6	B/G- B/R- G/R	37.14				53.19	-6.02	0.43	1.73	0.82	2.98
7	CB/B- CB/G- CB/R- B/G- B/R- G/R	668.64	516.10	-451.76	-9.92	611.50	-17.59	25.55	1.34	0.89	1.79
Integrated transform of S2A/MSI & L8/OLI											
8	B/G- B/R- G/R (S2A)	**989.63**	**490.07**	**-430.11**	**-9.28**	**359.42**	**-305.83**	**305.38**	**1.29**	**0.90**	**1.66**
	CB/B- CB/G- CB/R- B/G- B/R- G/R (L8)					**578.14**	**-14.52**	**21.79**			

Table 1. Calculated parameters for all combination of bands for linear, ratios, and cross-sensor-based transform methods. (The numbers highlighted in bold format are the values obtained for optimum method)

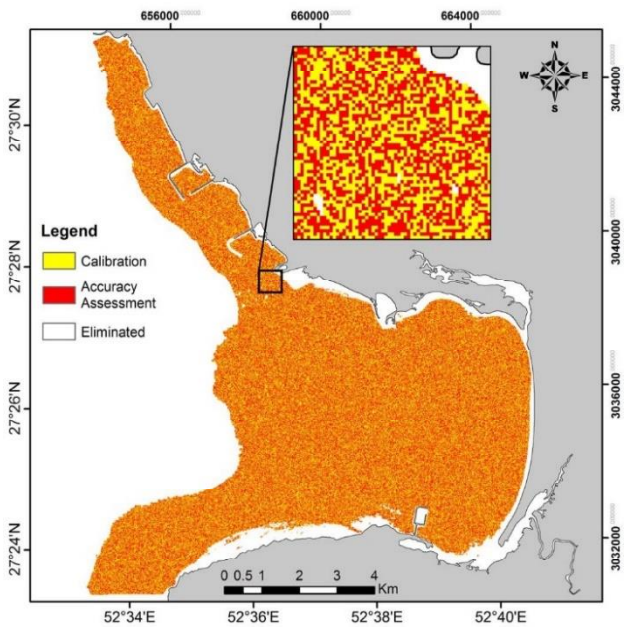

Figure 3. Randomly selected pixels from L8/OLI image to conduct calibration (red pixels) and accuracy assessment of the models (yellow pixels). The white pixels are the shallow areas or clouds that are masked from calculations.

3. RESULTS AND DISCUSSION

Table 1 summarize the calculated values of a_i and m_i parameters for all 8 aforesaid linear, ratio, and cross-sensor-based models. Moreover, the statistical indicators (including R^2, *SE*, and *RMSE*) are calculated from the data used for validation for both satellite images. The depth value for all chosen points for validation of the results were calculated by conducting the estimated values for unknown parameters and for all 8 selected models. Principally for the linear transformation, the yielded results demonstrated the optimum accuracy, in case of using all bands of both sensors, so that the statistical indices have shown this advancement (Model No. 4 in Table 1). In contrary, the lowest accuracy was detected when employing the RGB band of L8 image (Model No. 2 in Table 1). Although, adding CB band of Landsat imagery could increase the accuracy, it is still lower than cross-sensor-based model. On the other hand, the obtained results from the ratio transformation yielded the better accuracy for L8 sensor when all four bands were employed (Model No. 7 in Table 1), but for S2A/MSI sensor, the accuracy was increasingly lower than linear method (Model No. 5 in Table 1). Compared with the traditional linear and ratio transform methodologies, a significant improvement in the accuracy of the estimated depth values is observed when the cross-sensor-based transformation were utilized (Model No. 8 in Table 1). Although, the accuracy of integrated cross-sensor-band is not too high (R^2=0.9, *SE*=1.29, and *RMSE*=1.66), it is still valuable in absence of having precise bathymetric data for a specific area, particularly for benthic habitat mapping wit multispectral satellite data, when we need to have depth data to apply water column correction to enhance benthic habitats and coral reefs (Kabiri et al., 2013).

This contribution has been peer-reviewed. The double-blind peer-review was conducted on the basis of the full paper.
https://doi.org/10.5194/isprs-annals-X-4-W1-2022-343-2023 | © Author(s) 2023. CC BY 4.0 License.

This means that integration of the sensors may upgrade the accuracy by minimizing the remained errors after applying atmospheric corrections on raw images. Nevertheless, since the spatial resolution of L8/OLI images is 30 m in visible bands, it means that prior to run cross-sensor-based algorithm, it is necessary to downgrade the spatial resolution of S2A/MSI from 10 m to 30 m. Although, this reduction of spatial resolution seems to be critical at first glance, it can be negligible where the added improvements to our final results is quite significant. Moreover, it can be concluded that integration of harmonised L8/OLI and S2A/MSI imagers may minimize the errors which are usually come from atmospheric interferences, and consequently may increase the final estimated depth values. However, many studies showed that, in comparison with single image, the use of multi-temporal Sentinel-2 images may improve the estimated bathymetric data (Evagorou et al., 2019; Xu et al., 2021; Lumban-Gaol et al., 2022). It should be noted that Landsat-9 satellite has launched on September 2021with the same OLI imager and an 8-day time interval with Landsa-8 satellite. This means that the revisit cycle of having an image from a specific area will be 8 days, where the revisit cycle of both satellites is 16 days. This may highlight the advantages of the current study, where we can use our results and model on landsat-9 OLI imager as well.

Finally, it should be mentioned that according to the statistical indices for all models, the accuracy and precision of utilizing multispectral satellite imagery to estimate depth values are not that much that can be replaced with field measurements to generate hydrographic maps. As mentioned before, these depth data may be useful in absence of in situ data, where it is necessary to have relatively precise bathymetry data for mapping the benthic habitats or assessment of changes happened in the shallow coastal waters during the short or medium period of time. Moreover, it is important to mentioned that the estimated depth data with this method, cannot be used for navigation purposes where high precision data are necessary. However, the geometrical changes in bottom topography of benthic areas with medium or long period may be monitored by employing this method, where this is an important parameter for decision makers to management of benthic habitats and coastal areas.

ACKNOWLEDGMENT

[Iranian] National Cartographic Center (NCC) and [Iranian] Port and Maritime Organization (PMO) are acknowledged to prepare Hydrographic maps and bathymetric data from the study area. NASA, USGS, and ESA are acknowledged for preparing Landsat and Sentinel images. This study was partially supported by Iran National Science Foundation [grant no. INSF-99031644]. Dr. Khoshkholgh from INIOAS also is acknowledged for his supports to obtain bathymetric data.

REFERENCES

Baban, S.M., 1993. The evaluation of different algorithms for bathymetric charting of lakes using Landsat imagery. *International journal of remote sensing*, *14*(12), pp.2263-2273.

Beni, A.N., Marriner, N., Sharifi, A., Azizpour, J., Kabiri, K., Djamali, M. and Kirman, A., 2021. Climate change: A driver of future conflicts in the Persian Gulf Region?. *Heliyon*, *7*(2), p.e06288.

Chust, G., Grande, M., Galparsoro, I., Uriarte, A. and Borja, Á., 2010. Capabilities of the bathymetric Hawk Eye LiDAR for coastal habitat mapping: A case study within a Basque estuary. *Estuarine, Coastal and Shelf Science*, *89*(3), pp.200-213.

Clark, R.K., Fay, T.H. and Walker, C.L., 1987. Bathymetry calculations with Landsat 4 TM imagery under a generalized ratio assumption. *Applied optics*, *26*(19), pp.4036_1-4038.

Collin, A. and Planes, S., 2011, July. What is the value added of 4 bands within the submetric remote sensing of tropical coastscape? Quickbird-2 vs WorldView-2. In *2011 IEEE International Geoscience and Remote Sensing Symposium* (pp. 2165-2168). IEEE.

Eugenio, F., Marcello, J. and Martin, J., 2015. High-resolution maps of bathymetry and benthic habitats in shallow-water environments using multispectral remote sensing imagery. *IEEE Transactions on Geoscience and Remote Sensing*, *53*(7), pp.3539-3549.

Evagorou, E., Mettas, C., Agapiou, A., Themistocleous, K. and Hadjimitsis, D., 2019. Bathymetric maps from multi-temporal analysis of Sentinel-2 data: the case study of Limassol, Cyprus. *Advances in Geosciences*, *45*, pp.397-407.

Ghafarian, P., Kabiri, K., Delju, A.H. and Fallahi, M., 2022. Spatio-temporal variability of dust events in the northern Persian Gulf from 1991 to 2020. *Atmospheric Pollution Research*, *13*(4), p.101357.

Ghobadi, Y., Pradhan, B., Sayyad, G.A., Kabiri, K. and Falamarzi, Y., 2015a. Simulation of hydrological processes and effects of engineering projects on the Karkheh River Basin and its wetland using SWAT2009. *Quaternary International*, *374*, pp.144-153.

Ghobadi, Y., Pradhan, B., Shafri, H.Z., bin Ahmad, N. and Kabiri, K., 2015b. Spatio-temporal remotely sensed data for analysis of the shrinkage and shifting in the Al Hawizeh wetland. *Environmental monitoring and assessment*, *187*(1), pp.1-17.

Halls, J. and Costin, K., 2016. Submerged and emergent land cover and bathymetric mapping of estuarine habitats using worldView-2 and LiDAR imagery. *Remote Sensing*, *8*(9), p.718.

Horta, J., Pacheco, A., Moura, D. and Ferreira, Ó., 2014. Can recreational echosounder-chartplotter systems be used to perform accurate nearshore bathymetric surveys?. *Ocean Dynamics*, *64*(11), pp.1555-1567.

Kabiri, K. and Moradi, M., 2016. Landsat-8 imagery to estimate clarity in near-shore coastal waters: Feasibility study-Chabahar Bay, Iran. *Continental Shelf Research*, *125*, pp.44-53.

Kabiri, K., 2017. Accuracy assessment of near-shore bathymetry information retrieved from Landsat-8 imagery. *Earth Science Informatics*, *10*(2), pp.235-245.

Kabiri, K., 2017. DISCOVERING OPTIMUM METHOD TO EXTRACT DEPTH INFORMATION FOR NEARSHORE COASTAL WATERS FROM SENTINEL-2A IMAGERY-CASE STUDY: NAYBAND BAY, IRAN. *International Archives of the Photogrammetry, Remote Sensing & Spatial Information Sciences*, *42*.

Kabiri, K., 2020. Mapping coastal ecosystems and features using a low-cost standard drone: case study, Nayband Bay, Persian Gulf, Iran. *Journal of Coastal Conservation*, *24*(5), pp.1-8.

Kabiri, K., 2022a. Remote sensing of water clarity in the near-shore zone using a cross-sensor-based method: feasibility study: Kish Island, Persian Gulf. *Journal of Coastal Conservation*, *26*(4), pp.1-15.

Kabiri, K., 2022b. Estimation of the Secchi disk depth from the NASA MODIS-Aqua diffuse attenuation coefficient data in the northern Persian Gulf and the Gulf of Oman: A spatiotemporal assessment. *Regional Studies in Marine Science*, *52*, p.102359.

Kabiri, K., Pradhan, B., Samimi-Namin, K. and Moradi, M., 2013. Detecting coral bleaching, using QuickBird multi-temporal data: a feasibility study at Kish Island, the Persian Gulf. *Estuarine, Coastal and Shelf Science*, *117*, pp.273-281.

Kabiri, K., Rezai, H. and Moradi, M., 2018. Mapping of the corals around Hendorabi Island (Persian Gulf), using Worldview-2 standard imagery coupled with field observations. *Marine pollution bulletin*, *129*(1), pp.266-274.

Kabiri, K., Rezai, H. and Moradi, M., 2020. A drone-based method for mapping the coral reefs in the shallow coastal waters–case study: Kish Island, Persian Gulf. *Earth Science Informatics*, *13*(4), pp.1265-1274.

Kabiri, K., Rezai, H., Moradi, M. and Pourjomeh, F., 2014. Coral reefs mapping using parasailing aerial photography-feasibility study: Kish Island, Persian Gulf. *Journal of coastal conservation*, *18*(6), pp.691-699.

Liceaga-Correa, M.A. and Euan-Avila, J.I., 2002. Assessment of coral reef bathymetric mapping using visible Landsat Thematic Mapper data. *International Journal of Remote Sensing*, *23*(1), pp.3-14.

Lumban-Gaol, Y., Ohori, K.A. and Peters, R., 2022. Extracting Coastal Water Depths from Multi-Temporal Sentinel-2 Images Using Convolutional Neural Networks. *Marine Geodesy*, pp.1-30.

Lyzenga, D.R., 1978. Passive remote sensing techniques for mapping water depth and bottom features. *Applied optics*, *17*(3), pp.379-383.

Lyzenga, D.R., 1981. Remote sensing of bottom reflectance and water attenuation parameters in shallow water using aircraft and Landsat data. *International journal of remote sensing*, *2*(1), pp.71-82.

Maleika, Wojciech, Michal Palczynski, and Dariusz Frejlichowski. "Interpolation methods and the accuracy of bathymetric seabed models based on multibeam echosounder data." In *Asian Conference on Intelligent Information and Database Systems*, pp. 466-475. Springer, Berlin, Heidelberg, 2012.

Manessa, M.D.M., Kanno, A., Sekine, M., Haidar, M., Yamamoto, K., Imai, T. and Higuchi, T., 2016. Satellite-derived bathymetry using random forest algorithm and worldview-2 Imagery. *Geoplanning J Geomatics Plan*, *3*(117), pp.117-126.

Pacheco, A., Horta, J., Loureiro, C. and Ferreira, Ó., 2015. Retrieval of nearshore bathymetry from Landsat 8 images: A tool for coastal monitoring in shallow waters. *Remote Sensing of Environment*, *159*, pp.102-116.

Pahlevan, N., Lee, Z., Wei, J., Schaaf, C.B., Schott, J.R. and Berk, A., 2014. On-orbit radiometric characterization of OLI (Landsat-8) for applications in aquatic remote sensing. *Remote Sensing of Environment*, *154*, pp.272-284.

Samimi Namin, K., Rezai, H., Kabiri, K. and Zohari, Z., 2009. Unique coral community in the Persian Gulf. *Coral Reefs*, *28*(1), pp.27-27.

Saylam, K., Brown, R.A. and Hupp, J.R., 2017. Assessment of depth and turbidity with airborne Lidar bathymetry and multiband satellite imagery in shallow water bodies of the Alaskan North Slope. *International journal of applied earth observation and geoinformation*, *58*, pp.191-200.

Xu, N., Ma, X., Ma, Y., Zhao, P., Yang, J. and Wang, X.H., 2021. Deriving highly accurate shallow water bathymetry from Sentinel-2 and ICESat-2 datasets by a multitemporal stacking method. *IEEE Journal of Selected Topics in Applied Earth Observations and Remote Sensing*, *14*, pp.6677-6685.

Yunus, A.P., Dou, J., Song, X. and Avtar, R., 2019. Improved bathymetric mapping of coastal and lake environments using Sentinel-2 and Landsat-8 images. *Sensors*, *19*(12), p.2788.